A comparison of vortex and pseudo-spectral methods for the simulation of periodic vortical flows at high Reynolds numbers

Wim M. van Rees [a], Anthony Leonard [b], D.I. Pullin [b], Petros Koumoutsakos [a,*]

[a] Chair of Computational Science, ETH Zürich, CH-8092, Switzerland
[b] Graduate Aeronautical Laboratories, California Institute of Technology, Pasadena, CA 91125, USA

ARTICLE INFO

ABSTRACT

We present a validation study for the hybrid particle-mesh vortex method against a pseudo-spectral method for the Taylor–Green vortex at Re_Γ = 1600 as well as in the collision of two antiparallel vortex tubes at Re_Γ = 10,000. In this study we present diagnostics such as energy spectra and enstrophy as computed by both methods as well as point-wise comparisons of the vorticity field. Using a fourth order accurate kernel for interpolation between the particles and the mesh, the results of the hybrid vortex method and of the pseudo-spectral method agree well in both flow cases. For the Taylor–Green vortex, the vorticity contours computed by both methods around the time of the energy dissipation peak overlap. The energy spectrum shows that only the smallest length scales in the flow are not captured by the vortex method.

In the second flow case, where we compute the collision of two anti-parallel vortex tubes at Reynolds number 10,000, the vortex method results and the pseudo-spectral method results are in very good agreement up to and including the first reconnection of the tubes. The maximum error in the effective viscosity is about 2.5% for the vortex method and about 1% for the pseudo-spectral method. At later times the flows computed with the different methods show the same qualitative features, but the quantitative agreement on vortical structures is lost.

© 2010 Elsevier Inc. All rights reserved.

1. Background

Vortex methods are arguably the first numerical method used for the simulation of vortical flows starting with the hand-calculations of Rosenhead in the beginning of last century [1]. Vortex methods were considered as the method of choice for external flows with compact vorticity [2] due to their low numerical dissipation and they were among the first techniques used for simulations of 3D vortical flows [3–5]. In recent years it was realized [6] that the accuracy of the method hinges on the use of a regularisation procedure to remedy the inaccuracies due to the distortion of the computational elements which follows from their Lagrangian adaptivity. In the remeshed vortex method (rVM) [7–9], Lagrangian vortex particles are used to simulate the convective part of the equations and particles are mapped onto grid nodes at each time step so as to ensure the convergence of the method and to compute efficiently the solution of the Poisson equation that determines their velocity. This gives the rVM some inherent advantages over other methods, such as its adaptivity and the lack of a CFL restriction on the timestep, which allows large timesteps during the simulation. It is important to note that the use of a grid based solver for the Poisson equation accommodates a wide range of boundary conditions that may not be possible when using tech-

---

niques such as the Fast Multipole Method [10]. We are interesting in exploiting these advantages for high Reynolds number (Re_Γ = 10,000) vortical flows while retaining the accuracy of the results. The method has already successfully been used to perform direct numerical simulations up to Re_Γ = 7500 [11,12]. To this end, we will compare our remeshed vortex method with a pseudo-spectral method. The pseudo-spectral method is well suited for the simulation of high Reynolds number flows in simple domains and can be considered as a reference method. The goal of the current study is to validate the vortex method as an accurate and fast alternative to the pseudo-spectral method for high Reynolds number flow cases.

The first study of comparing the vortex method with the pseudo-spectral method was undertaken by Cottet et al. [13]. In that study, the comparison was performed for isotropic turbulence in a periodic box at initial $Re_\lambda \approx 100$, and for the reconnection of two vortex tubes at Re_Γ = 3500. In the last case the flow was still laminar. For both cases it was found that the vortex method resolves the large- and medium scales in the flow well. In addition, the simulation of isotropic turbulence showed that the vortex method does not suffer from accumulation of energy in the tail of the energy spectrum, whereas the spectral method does. Furthermore, an underresolved flow simulation of the colliding vortex tubes showed that the pseudo-spectral method generates spurious vortex structures, but with the vortex method the large scales are still adequately resolved and no spurious vorticity appears. In a recent work by Cocle et al. [14] a vortex method and a pseudo-spectral code are used to compare various multiscale subgrid models in LES of homogeneous isotropic turbulence. They report little difference between the two methods in the obtained spectra when using the same subgrid model.

In this study we focus on the accuracy of the vortex method at higher Reynolds numbers than in [13], and we study the effect of employing a higher order remeshing kernel in the remeshed vortex method. The paper is organized as follows. First we describe the methods used in this study. Then we report on the simulation results for a Taylor–Green vortex at Re_Γ = 1600. Finally we move on to a flow case at Re_Γ = 10,000 and describe the comparison between the vortex method results and the pseudo-spectral method results.

2. Governing equations and numerical method

2.1. Vortex method

The evolution of viscous incompressible flow is considered as described by the Navier–Stokes equations in Lagrangian vorticity form:

$$\frac{D\boldsymbol{\omega}}{Dt} = (\boldsymbol{\omega} \cdot \nabla)\mathbf{u} + v\Delta\boldsymbol{\omega}, \tag{1}$$

and

$$\Delta\boldsymbol{\Psi} = \nabla \times \mathbf{u} = -\boldsymbol{\omega}, \tag{2}$$

where $\boldsymbol{\Psi}$ is the vector streamfunction.

The equations are discretized using a remeshed vortex method (rVM). In the traditional vortex particle method, the vorticity field is approximated using particles:

$$\boldsymbol{\omega}(\mathbf{x}, t) \approx \sum_p \boldsymbol{\Gamma}_p(t)\zeta_\epsilon(\mathbf{x} - \mathbf{x}_p(t)), \tag{3}$$

where $\boldsymbol{\Gamma}_p(t)$ and $\mathbf{x}_p(t)$ denote the particle strength and particle position, respectively, of the pth particle at time t. In our hybrid formulation of the vortex particle method, the kernel function ζ_ϵ is used for interpolation between the particles and the grid (see the next subsection). To compute the Fourier-transform of our quantities, we assume a Fourier interpolation on the grid rather than using Eq. (3).

Discretizing the Navier–Stokes equations with particles results in a set of ordinary differential equations (ODEs) for the particle strengths and the particle positions:

$$\frac{d\boldsymbol{\Gamma}_p}{dt} = v_p(\boldsymbol{\omega} \cdot \nabla^h)\mathbf{u} + v\Delta^h\boldsymbol{\Gamma}_p, \tag{4}$$

$$\frac{d\mathbf{x}_p}{dt} = \mathbf{u}(\mathbf{x}_p, t). \tag{5}$$

Here $v_p = h^3$ are the particle volumes. These differential equations are integrated in time using either a low-storage third order Runge–Kutta method [15] (RK3), or a fourth order Runge–Kutta method (RK4). The discretized operator for the viscous term is evaluated with a centered fourth-order finite difference scheme. The stretching term is rewritten in its transpose formulation $\omega_k \partial u_k / \partial x_i$, and is discretized with fourth order finite differences. Every timestep the particles are remeshed onto a uniform Cartesian grid to enforce that the particles always overlap. In this way the occurrence of spurious vortical structures is prevented and convergence of the method is ensured [16,7]. The velocities are computed from the vorticity by solving Eq. (2) in Fourier space on the grid. This ensures that the velocity field is spectrally divergence-free. To ensure a divergence-free vorticity field ($\nabla \cdot \boldsymbol{\omega} = 0$), a solenoidal reprojection based on the Helmholtz decomposition of the vorticity field is done in spectral space every 5–10 timesteps.

The timestep varies during the computation according to the deformation in the flow. Specifically, with the deformation tensor defined as $S = \frac{1}{2}(\nabla \mathbf{u} + (\nabla \mathbf{u})^T)$, then the timestep according to the deformation criterion is given by the one-norm of S:

$$\delta t = \text{LCFL}\left(\max_{1 \leqslant j \leqslant 3} \sum_{i=1}^{3} |S_{ij}| \right)^{-1}, \tag{6}$$

where LCFL is a user-controlled parameter. This measure bounds the deformation rate in the flow. A second criterion on the timestep is given by the Fourier number and relates to the stability of the diffusion term discretized on the mesh. For high Reynolds number flows the magnitude of the timestep is dominated by the deformation measure.

The vortex code is a parallel application implemented as a client of the Parallel Particle Mesh (PPM) library [17].

2.2. Kernel function for vortex method

In our method, we use the particle kernel function $\zeta_\epsilon(\mathbf{x} - \mathbf{x}_p(t))$ for the interpolation between the particle and the mesh. We use $\epsilon = h$, where h is the spacing of the (uniform) grid. A commonly used kernel in particle methods is the M'_4 kernel [18,6,8], defined as:

$$M'_4(x) = \begin{cases} 0 & \text{if } |x| > 2, \\ \frac{1}{2}(2 - |x|)^2(1 - |x|) & \text{if } 1 < |x| \leqslant 2, \\ 1 - \frac{5x^2}{2} + \frac{3|x|^3}{2} & \text{if } |x| \leqslant 1. \end{cases} \tag{7}$$

This kernel has a four-point support and has an error of $\mathcal{O}(h^3)$. In addition to the M'_4 kernel, we will use a kernel derived in [19], denoted as the M^*_6 kernel. This kernel has a support of six points and has an error of $\mathcal{O}(h^4)$. It is defined by:

$$M^*_6(x) = \begin{cases} 0 & \text{if } |x| > 3, \\ -\frac{1}{24}(|x| - 2)(|x| - 3)^3(5|x| - 8) & \text{if } 2 < |x| \leqslant 3, \\ \frac{1}{24}(|x| - 1)(|x| - 2)(25|x|^3 - 114x^2 + 153|x| - 48) & \text{if } 1 < |x| \leqslant 2, \\ -\frac{1}{12}(|x| - 1)(25x^4 - 38|x|^3 - 3x^2 + 12|x| + 12) & \text{if } |x| \leqslant 1. \end{cases} \tag{8}$$

Both kernels are plotted in Fig. 1. In three dimensions we use the tensorial product of the above interpolation kernels. From here on, we will denote the remeshed vortex method with the M'_4 interpolation kernel as rVM-M'_4, the remeshed vortex method with the M^*_6 interpolation kernel as rVM-M^*_6 and the pseudo-spectral method as PS.

2.3. Pseudo-spectral method

We employ a standard pseudo-spectral method (PS) using a fourth order Runge–Kutta method for timestepping. The Navier–Stokes equations for the vorticity are solved in the rotational formulation:

$$\frac{\partial \boldsymbol{\omega}}{\partial t} = \nabla \times (\mathbf{u} \times \boldsymbol{\omega}) + v \Delta \boldsymbol{\omega}, \tag{9}$$
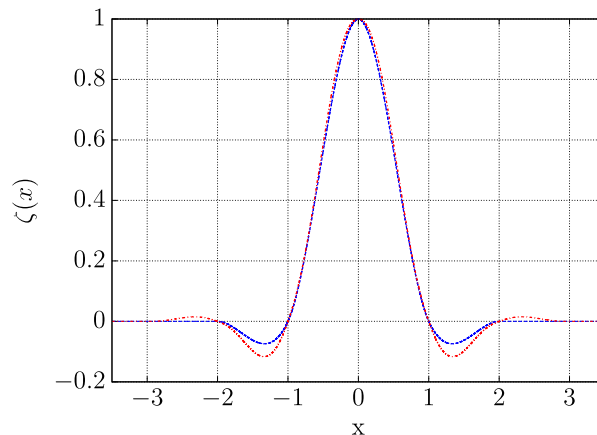
Fig. 1. The third order M'_4 kernel (dashed blue) and the fourth order M^*_6 kernel (dashed-dotted red) used for remeshing the particles onto the mesh in the rVM. (For interpretation of the references to colour in this figure legend, the reader is referred to the web version of this article.)

together with the Poisson equation for the velocity given in Eq. (2). The rotational formulation ensures that the vorticity field remains divergence-free for the duration of the computation. De-aliasing is done with the smooth truncation formula described in [20]. For more details on the pseudo-spectral method, see [21–23]. All pseudo-spectral simulations are performed with a constant CFL-number of 0.75. Like the vortex-particle method, our pseudo-spectral solver is implemented as a client of the PPM-library and exploits the scaling capacities of this library.

3. Taylor–Green vortex

The Taylor–Green vortex is a benchmark flow case that is often used to study the generation of small-scale vorticity and small-scale vortical structures from a smooth initial condition under the influence of vortex stretching (e.g. [24]). The family of initial conditions, defined in a periodic cube with side length 2π, are described by the following equations:

$$u_x(\mathbf{x}, t = 0) = \frac{2}{\sqrt{3}} \sin\left(\theta + \frac{2\pi}{3}\right) \sin(x) \cos(y) \cos(z),$$

$$u_y(\mathbf{x}, t = 0) = \frac{2}{\sqrt{3}} \sin\left(\theta - \frac{2\pi}{3}\right) \cos(x) \sin(y) \cos(z),$$

$$u_z(\mathbf{x}, t = 0) = \frac{2}{\sqrt{3}} \sin(\theta) \cos(x) \cos(y) \sin(z).$$

(10)

Here θ is the free parameter, and it is set to $\theta = 0$ for all results in this study. The Reynolds number in this flow is defined as $Re_\Gamma = 1/v$ and in this work we set it equal to $Re_\Gamma = 1600$. The time integration for the vortex method is done with a third order Runge–Kutta method with the timestep determined by the minimum of the advection-based criterion, here LCFL = 0.125, and the diffusion based criterion as determined by the Fourier number. For the pseudo-spectral method we employ a fourth order Runge–Kutta time integration with CFL = 0.75.

We performed the computation with the rVM-M_4', the rVM-M_6^* and the PS, using resolutions of 256^3, 512^3 and 768^3. The 256^3 resolution results are relevant as they shows how close the vortex method approximates the pseudo-spectral results for an underresolved computation. At a resolution of 512^3 the pseudo-spectral method has converged. For each resolution we compare the vortex method results with the pseudo-spectral method results in the next subsections.

3.1. Comparison at 256^3 resolution

Fig. 2 shows the evolution of the dissipation as a function of time. Up to $T \approx 6.5$, the rVM-M_6^* results are on top of the PS results, whereas the results from the rVM-M_4' slightly underpredict the dissipation. For larger times, the rVM-M_6^* results show a consistent larger dissipation than the PS results, although the shape of these two curves are qualitatively similar. In the close-up of the region $7.5 \leqslant T \leqslant 10.0$ it can clearly be seen that the rVM-M_6^* overpredicts the dissipation peak, whereas with the rVM-M_4' the dissipation peak is underpredicted with respect to the PS. Fig. 6(a) shows the tail of the energy spectrum for all three methods at $T = 9.0$. The drop in energy at the highest wavenumbers in the pseudo-spectral method is due to

(a) overview   (b) close-up of region $7.5 \leq t \leq 10$
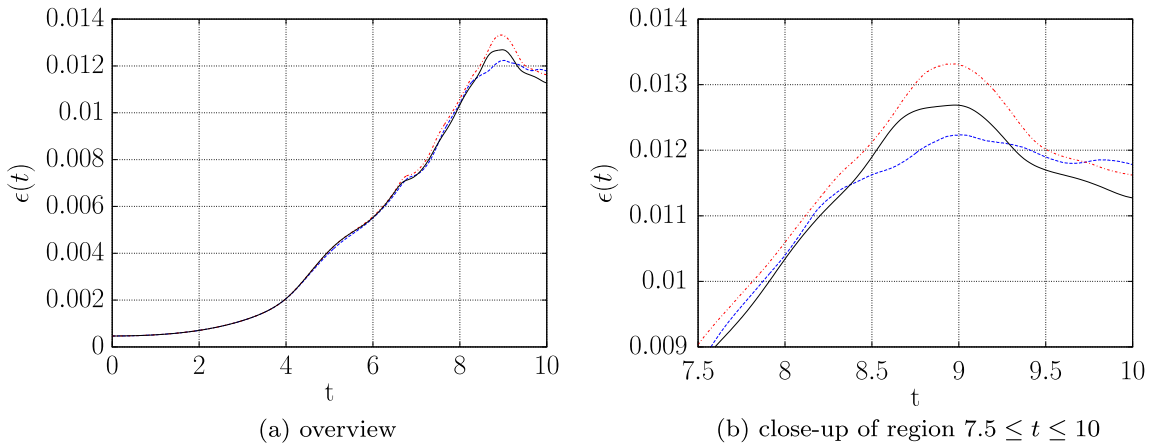
Fig. 2. Energy dissipation of Taylor–Green vortex as a function of time, $Re_\Gamma = 1600$, the resolution is 256^3 for all methods. PS results (solid black) compared with the rVM-M_4' results (long dashed blue) and with the rVM-M_6^* results (dash-dotted red). (For interpretation of the references to colour in this figure legend, the reader is referred to the web version of this article.)

the smoothing filter used for dealiasing, as mentioned above. We can see that in the high-end of the wavespectrum, the rVM-M_6^* slightly overpredicts the energy in the highest wavenumbers, whereas the rVM-M_4' underpredicts the energy.

3.2. Comparison at 512^3 resolution

The Taylor–Green flow has been computed for all methods with a resolution of 512^3. In Fig. 3 the evolution of the energy dissipation as a function of time is given for the rVM-M_4', for the rVM-M_6^* and for the PS. We see that the rVM-M_4' at this higher resolution compares much better against the pseudo-spectral method, up to $T \approx 8.5$ there is a maximum difference between the two methods of 0.8%. Just like in the low-resolution case, the dissipation computed with the rVM-M_4' is consistently lower than the dissipation computed with the PS. Beyond $T \approx 8.5$ the deviation between the two methods increases as shown in the right pane of Fig. 3. Fig. 4 shows the contours of maximum vorticity in the $x = 0$ plane for both the PS and the rVM-M_4', both at the same resolution of 512^3. The contour lines at $T = 8.0$ show that the flow computed by the vortex method approaches the pseudo-spectral flow, but visible discrepancies remain. One example is the overprediction of the vortex structure by the vortex method in the center bottom of Fig. 4(a). At $T = 9.0$ the differences between the two methods have increased further.

The comparison of the results from the rVM-M_6^* with the PS results shows that the vortex method benefits greatly from the higher order kernel. The evolution of energy dissipation (Fig. 3) is virtually indistinguishable between the two methods, in the range $0 \leqslant T \leqslant 10$ the maximum difference between the M_6^* dissipation and the pseudo-spectral dissipation is 0.27%, occurring at time $T = 9.82$. Comparing the contours of vorticity magnitude (see Fig. 5) we see that the contour lines corresponding to higher vorticity values are indistinguishable. For the lower vorticity values some small differences persist (notice that the contour corresponding to the earlier mentioned vortex structure in the center bottom part of the plot at $T = 8.0$ persists for the M_6^*-kernel computation), but overall the flow computed with the rVM-M_6^* agrees well with the PS results.

In Fig. 7(a) we show the highest wavenumbers of the energy spectrum at $T = 9.0$ for the methods at resolution 512^3. We can see that compared with the M_4'-kernel, the vortex method results with the M_6^*-kernel follow the pseudo-spectral results much closer in the range $100 \leqslant k \leqslant 200$. For wavenumbers $k > 200$ some differences start to appear. Since the pseudo-spectral method results are affected by the truncation (see the 'hump' in the energy spectrum just before it drops), we cannot tell which method produces the more accurate energy spectrum in this regime.

3.3. Comparison at 768^3 resolution

Fig. 8 shows the dissipation evolution for the three methods at the highest resolution. The results for the vortex method with M_6^* kernel and the pseudo-spectral method overlap. The rVM-M_4', however, still slightly underpredicts the dissipation peak (see close-up). The contour lines of all three flows are plotted in Fig. 9 for times $T = 8.0$ and $T = 9.0$. There is a minimal visual discrepancy between the rVM-M_6^* and the PS, only in the contour of the smallest vorticity some differences are visible. For the rVM-M_4' there is still a small difference present, which can only be explained by the lack of spatial accuracy of the interpolation kernel, even at a resolution of the background grid of 768^3.

The Taylor–Green simulations show that the rVM-M_6^* is able to capture a significant amount of flow scales and its accuracy approaches the accuracy of a spectral method for this specific flow-scenario. We will apply these results to a high Reynolds number simulation of a vortical flow in the next section.

(a) overview   (b) close-up of region $7.5 \leq t \leq 10$
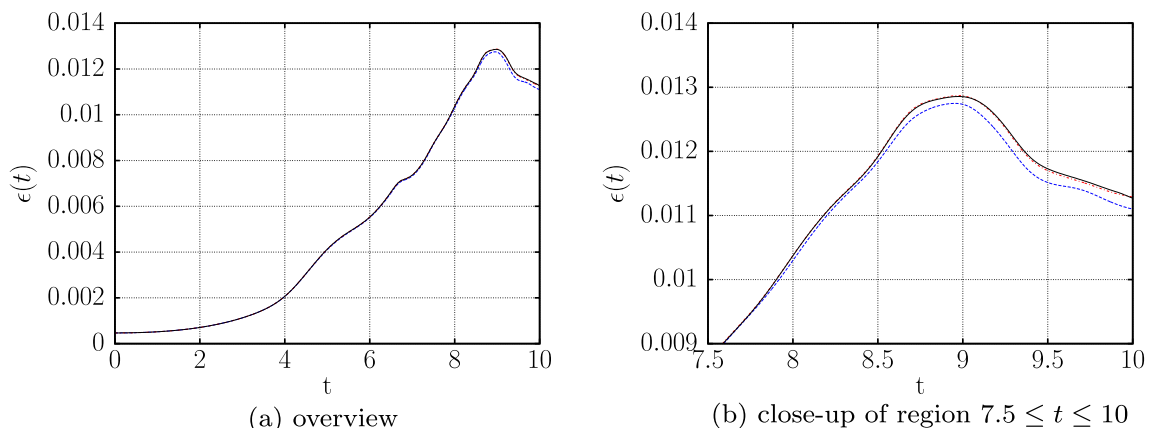
Fig. 3. Energy dissipation of Taylor–Green vortex as a function of time, $Re_\Gamma = 1600$, the resolution is 512^3 for all methods. PS results (solid black) compared with the rVM-M_4' results (long dashed blue) and with the rVM-M_6^* results (dash-dotted red). (For interpretation of the references to colour in this figure legend, the reader is referred to the web version of this article.)
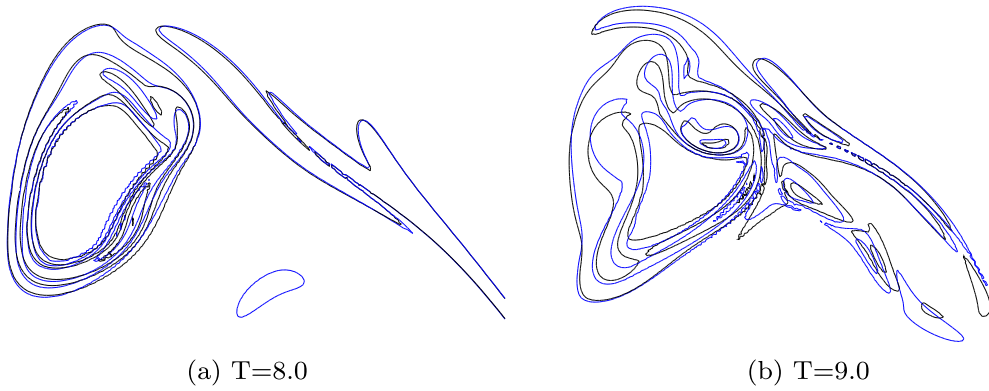
Fig. 4. Contours of $|\omega|$ in the $x = 0$ plane of the Taylor–Green vortex at $Re_\Gamma = 1600$. Shown are the PS results (black) and the rVM-M_4' results (blue), both with 512^3 resolution. The contours plotted are for $|\omega|$ values of 1, 5, 10, 20, 30. (For interpretation of the references to colour in this figure legend, the reader is referred to the web version of this article.)
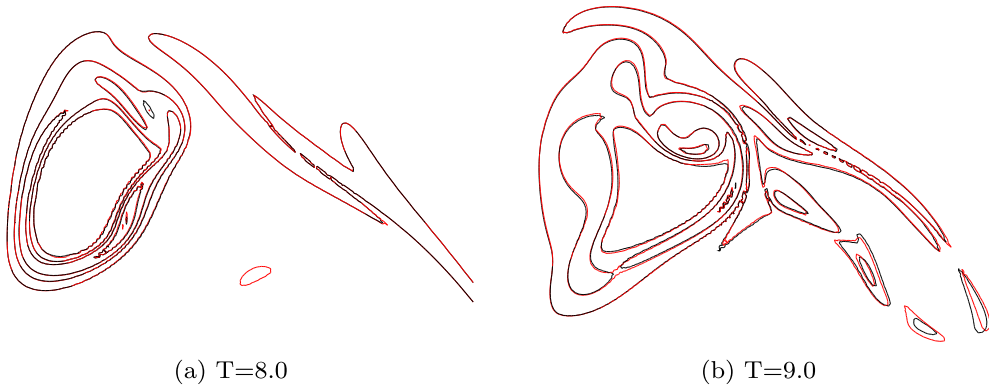
Fig. 5. Contours of $|\omega|$ in the $x = 0$ plane of the Taylor–Green vortex at $Re_\Gamma = 1600$. Shown are the PS results (black) and the rVM-M_6^* results (red), both with 512^3 resolution. The contours plotted are for $|\omega|$ values of 1, 5, 10, 20, 30. (For interpretation of the references to colour in this figure legend, the reader is referred to the web version of this article.)
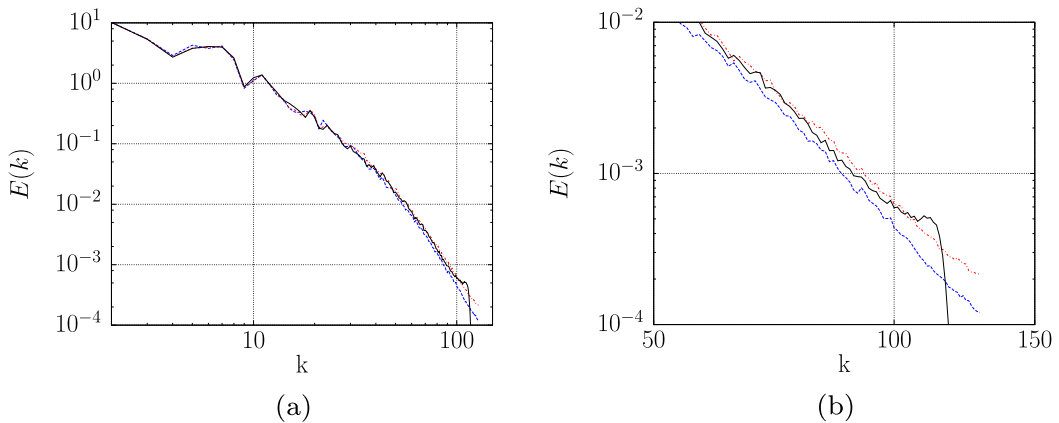
Fig. 6. Comparison of the complete energy spectrum of the Taylor–Green vortex at $Re_\Gamma = 1600$, at $T = 9.0$ for 256^3 (left), and zoom in at the tail (right). Plotted are the PS results (solid black), the rVM-M_4' results (long dashed blue) and the rVM-M_6^* results (dash-dotted red). (For interpretation of the references to colour in this figure legend, the reader is referred to the web version of this article.)
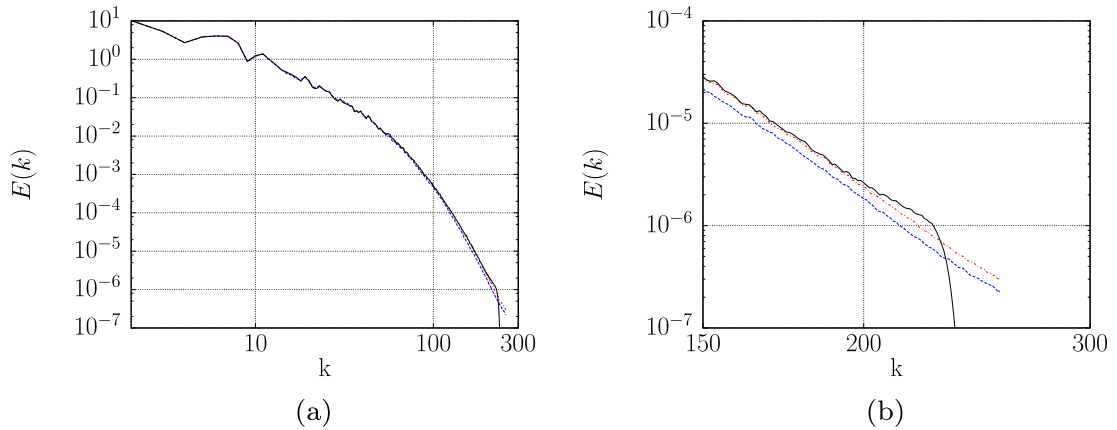
Fig. 7. Comparison of the complete energy spectrum of the Taylor–Green vortex at $Re_\Gamma = 1600$, at $T = 9.0$ for 512^3 (left), and zoom in at the tail (right). Plotted are the PS results (solid black), the rVM-M_4' results (long dashed blue) and the rVM-M_6^* results (dash-dotted red). (For interpretation of the references to colour in this figure legend, the reader is referred to the web version of this article.)
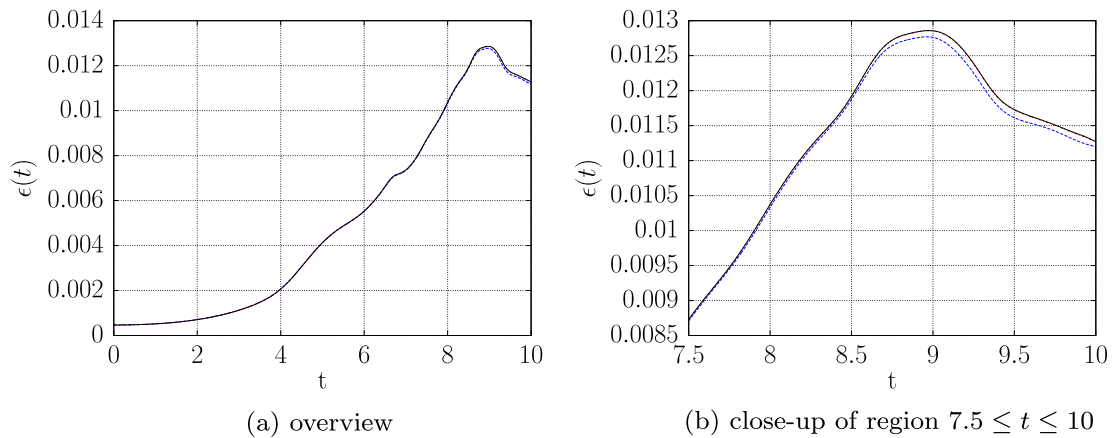
Fig. 8. Energy dissipation of Taylor–Green vortex as a function of time, $Re_\Gamma = 1600$, the resolution is 768^3 for all methods. PS results (solid black) compared with the rVM-M_4' results (long dashed blue) and with the rVM-M_6^* results (dash-dotted red). (For interpretation of the references to colour in this figure legend, the reader is referred to the web version of this article.)
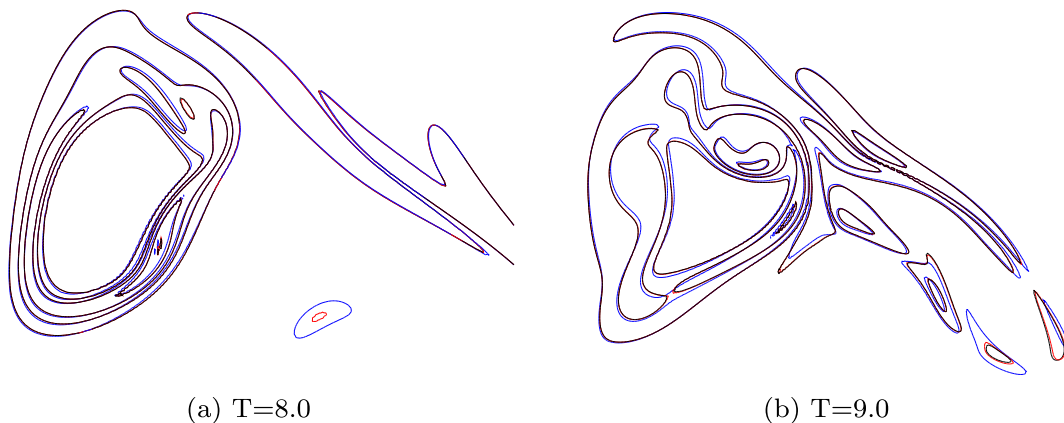
Fig. 9. Contours of $|\omega|$ in the $x = 0$ plane of the Taylor–Green vortex at $Re_\Gamma = 1600$. Shown are the PS results (black), the rVM-M_4' results (blue) and the rVM-M_6^* results (red), all with 768^3 resolution. The contours plotted are for $|\omega|$ values of 1, 5, 10, 20, 30. (For interpretation of the references to colour in this figure legend, the reader is referred to the web version of this article.)

4. Collision of two vortex tubes

We consider the flow evolving from two perturbed vortex tubes starting side by side in a periodic domain, for a Reynolds number based on the initial circulation of one vortex tubes of $Re_\Gamma = 10,000$. This flow case exhibits many features which are common to turbulent flows such as vorticity topology change, a strong production of small-scale vorticity and its dissipation in the high-wavenumber range.

In a domain with size $[6\pi \times 4\pi \times 2\pi]$, the vortex tubes are initialized in a configuration commonly used in literature, e.g. [25–27]. Specifically, we define the vorticity profile in the core as an axisymmetric function $\omega(r)$ as follows:

$$\omega(r) = \begin{cases} \omega_0 \left[1 - \exp\left(-\frac{K}{r^*} \exp\left(\frac{1}{r^*-1} \right) \right) \right] & \text{if } r^* < 1, \\ 0 & \text{else,} \end{cases} \tag{11}$$

where $r^* = r/r_{\text{cutoff}}$ and the factor K is defined as $K = 1/2 \exp(2) \log(2)$. Following [25], we choose $r_{\text{cutoff}} = 0.666$ for our setup.

Along the z-direction the tubes are sinusoidally perturbed with an amplitude A at an inward inclination angle α. For the vortex tube in the negative half of the x-plane, the distance to the core is defined as:

$$r(\mathbf{x})^2 = [x - (x_c + A\cos(\alpha)(1 + \cos(z)))]^2 + [y - (y_c + A\sin(\alpha)(1 + \cos(z)))]^2, \tag{12}$$

where $x_c + 2A\cos(\alpha)$ and $y_c + 2A\sin(\alpha)$ are the x and y-coordinates of the center of the vortex tube in the $z = 0$ plane.

The vorticity field corresponding to this tube is then given by:

$$\boldsymbol{\omega}(\mathbf{x}) = \omega(r)(-A\cos(\alpha)\sin(z)\hat{\mathbf{x}} - A\sin(\alpha)\sin(z)\hat{\mathbf{y}} + \hat{\mathbf{z}}). \tag{13}$$

Here $\hat{\mathbf{x}}$, $\hat{\mathbf{y}}$ and $\hat{\mathbf{z}}$ are the unit vectors in x, y and z directions, respectively.

The space between the unperturbed tubes in the $z = \pi$-plane is 1.732. We set $y_c = 0$ for both tubes, while $x_c = -0.866$ for the tube described above and $x_c = 0.866$ for the other tube. The perturbation amplitude is equal to $A = 0.2$ and the inclination angle of the tubes in the xy-plane, with respect to the y-axis, is equal to $\alpha = \pi/3$ for the tube in the negative half of the x-plane and $\alpha = 2\pi/3$ for the other. We evolve the flow with $\nu = 0.001$ and set $\omega_0 = 26.093$ to achieve a Reynolds number based on the initial circulation in the cross-section of one of the tubes equal to $Re_\Gamma = 10,000$. Finally, after initialization, we perform a spectral solenoidal reprojection of the vorticity field.

Starting from these initial conditions, we evolve the flow three times: once with the PS, once with the rVM-M'_4 and once with the rVM-M^*_6. In all cases the resolution of the grid is equal to $[1280 \times 960 \times 640]$ points. For the PS computations we choose a constant CFL = 0.75. In the computation with the rVM-M'_4 we use our RK3 time integration with LCFL = 0.0625. For the rVM-M^*_6 computations we use a RK4 time integration with LCFL = 0.125. Each computation was done on 4096 cores on a Cray XT5 system at the Swiss National Supercomputer Center (CSCS).

4.1. Comparison between the pseudo-spectral method and the vortex method

Here we compare several diagnostics as well as flow visualizations at specific times between the vortex method results and the pseudo-spectral results. A measure of the accuracy of the computations at any point in time is provided by the effective viscosity of the flow. From integrating the evolution equation of the kinetic energy in the flow over the computational domain, it follows that [28]

(a) Relative effective viscosity   (b) Enstrophy evolution
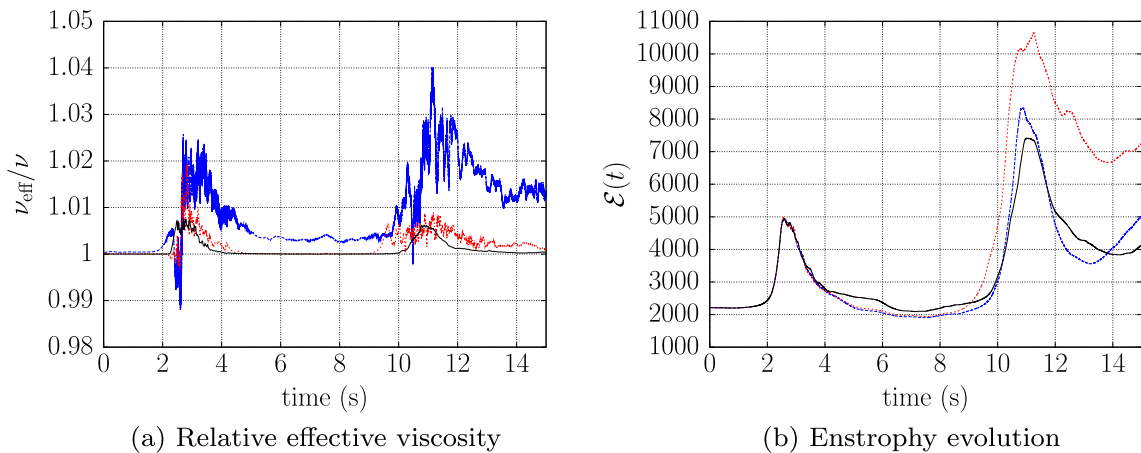
Fig. 10. Comparison of the relative effective viscosity and the total enstrophy over time. PS (solid black), rVM-M'_4 (dashed blue) and rVM-M^*_6 (dotted red). (For interpretation of the references to colour in this figure legend, the reader is referred to the web version of this article.)

$$\frac{\mathrm{d}E}{\mathrm{d}t} = -\nu\mathscr{E}, \qquad (14)$$

where $\mathscr{E} = \int \boldsymbol{\omega} \cdot \boldsymbol{\omega} \,\mathrm{d}\mathbf{x}$ is the enstrophy and E is the kinetic energy. The effective viscosity can then be defined by

$$\nu_{\mathrm{effective}} = -\frac{\mathrm{d}E}{\mathrm{d}t} / \mathscr{E}. \qquad (15)$$

The energy and enstrophy are computed from the velocity and vorticity on the mesh, respectively. We compare the effective viscosity to the actual viscosity in the flow to measure the error.

The results for the computations are given in Fig. 10(a), where we divided the effective viscosity by the physical viscosity $\nu = 0.001$ to study the relative differences. The maximum error in effective viscosity is about 4% and 2.5% for the rVM-M'_4 and the rVM-M^*_6, respectively, and about 1% for the pseudo-spectral method. An interesting element of this plot is that the vortex method, with both the M'_4 and the M^*_6 kernels, gives a relative effective viscosity smaller than 1 during some parts of the flow evolution. This means that our method is less dissipative than it should be according to the physical viscosity of the flow in these parts of the computation, and that we are actually computing at a slightly larger effective Reynolds number than the physical Reynolds number. The pseudo-spectral method, on the other hand, has a relative effective viscosity which is always larger than 1.

Fig. 10(b) gives the total enstrophy in the flow compared between the three methods. Up to and including the first reconnection ($T \leqslant 4.0$) the three methods show qualitatively similar behavior. This is confirmed when comparing snapshots of the flow during the first reconnection (Fig. 11). The flow visualization shows that the M^*_6-kernel resolves more scales than the
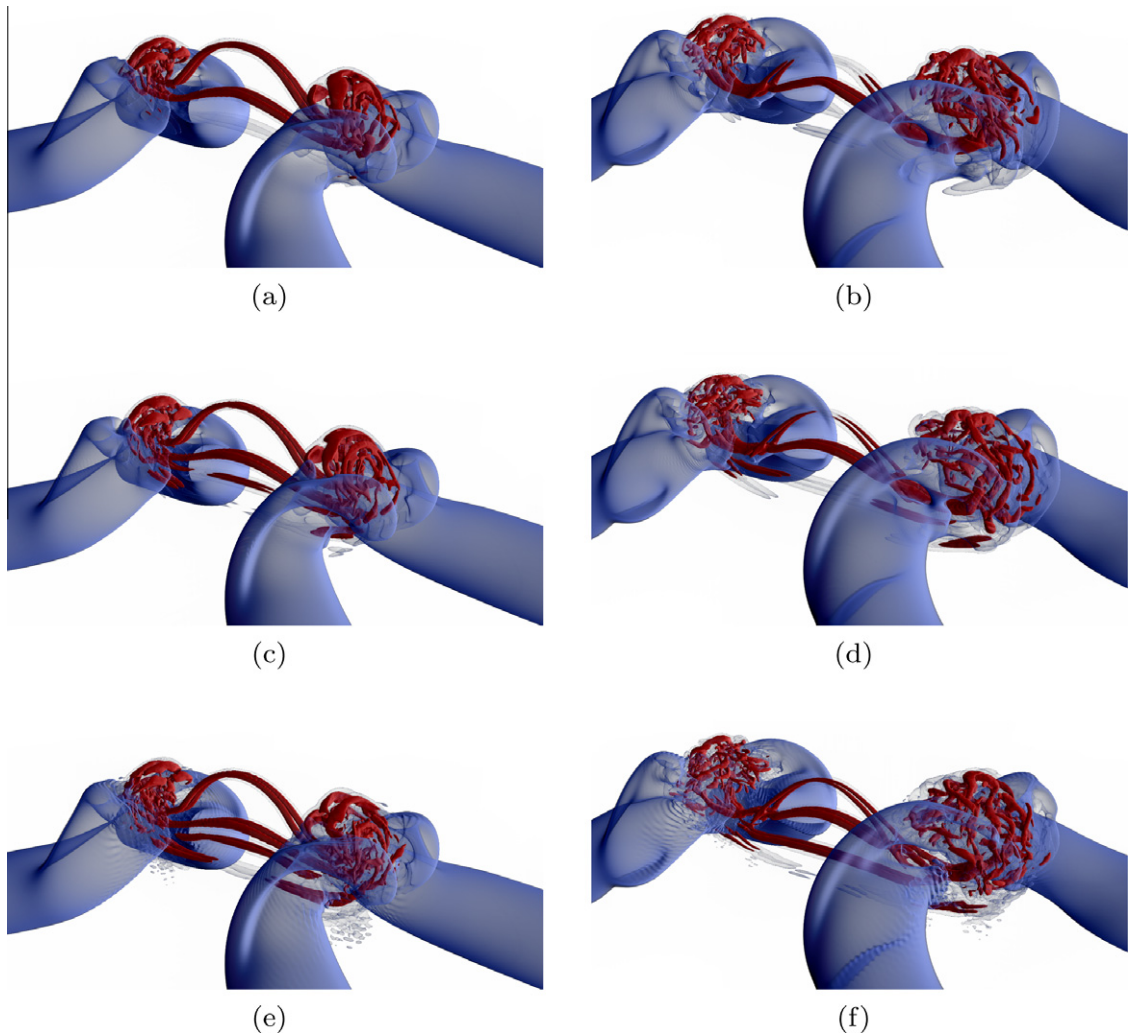
Fig. 11. Visualization of the flow at time $T = 2.65$ (a), (c), (e) and at time $T = 2.85$ (b), (d), (f). Results predicted with rVM-M'_4 (a), (b), with rVM-M^*_6 (c), (d) and with PS (e), (f). The figure is a volume rendering of the λ_2-field [29].

M_4'-kernel, although still differences with respect to the pseudo-spectral method can be seen. At times greater than approximately 4.0, we see that the vortex method results start to diverge from the PS results. In Fig. 12 we visualize the flow around $t = 11$, during the second reconnection. We see that the second reconnection starts earlier for the rVM-M_6^*. Therefore in the left pane of Fig. 12 we see that the reconnection is further developed for the rVM-M_6^* results compared with the other results. However, we should not forget that we are simulating a high Reynolds number flow initialized without noise. This means that small differences in the flow at one point in time can lead to very different flow evolutions later in time. Given the evolution of the effective viscosity (Fig. 10(a)) the rVM-M_6^* still approximates the Navier–Stokes equations with a smaller error than the rVM-M_4', so we can conclude that for later times the comparison between the different results should not be given too much importance.

4.2. Timings

For the particular case of the colliding vortex tubes, we compare the timings between the pseudo-spectral method and the vortex method. As mentioned before, the implementation of the FFTs used in our pseudo-spectral method is the same as the FFTs used in the vortex method. Table 1 presents the results. The additional cost of the vortex method with RK4 algorithm over the pseudo-spectral method is because of the particle operation, predominantly particle mapping and particle interpolation. The difference is small, however, because the pseudo-spectral method needs to FFT more fields per substep of the algorithm. Each substep, the vortex method forward-transforms the vorticity and backward-transforms the velocity,

(a)

(b)

(c)

(d)

(e)

(f)
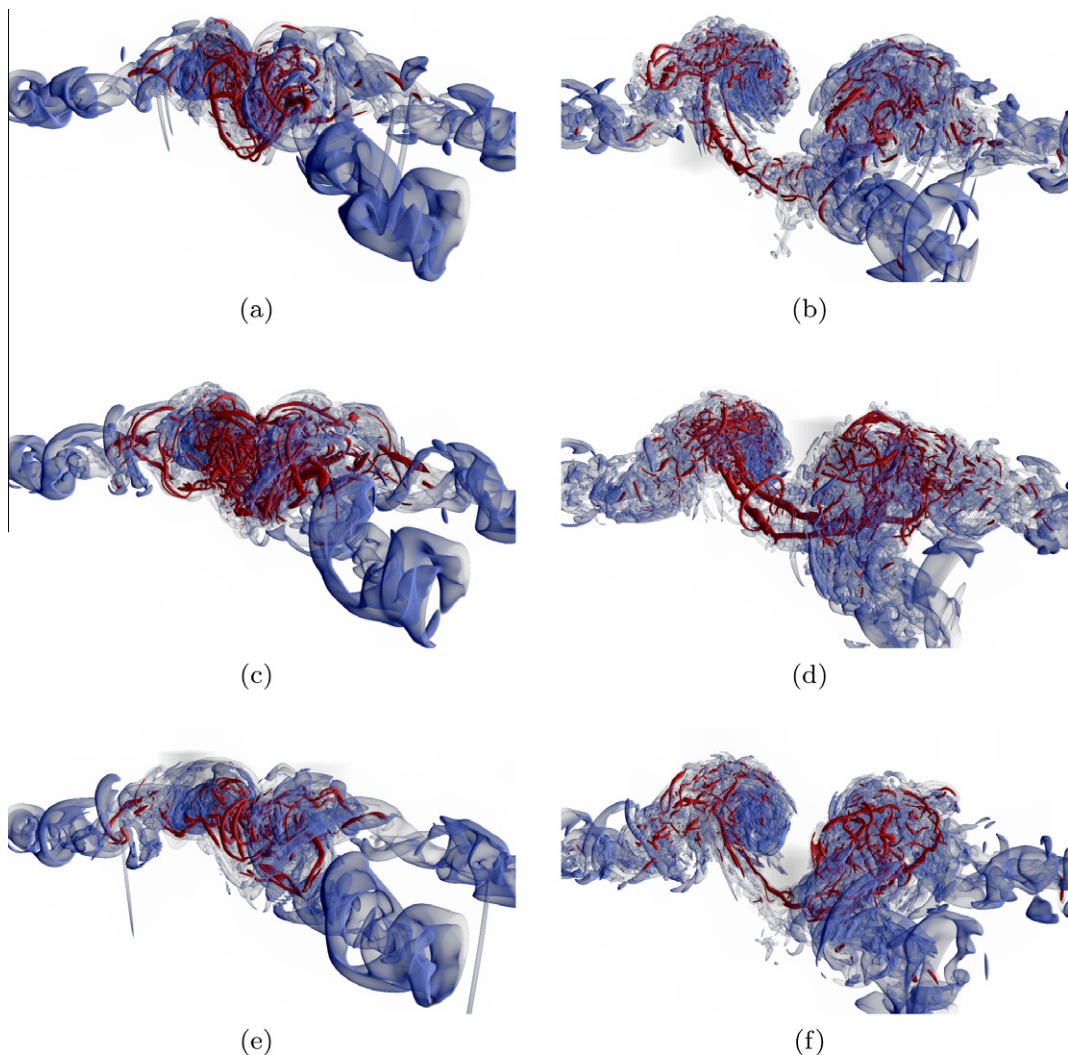
Fig. 12. Visualization of the flow at time $T = 10.5$ (a), (c), (e) and at time $T = 11.5$ (b), (d), (f). Results predicted with rVM-M_4' (a), (b), with rVM-M_6^* (c), (d) and with PS (e), (f). The figure is a volume rendering of the λ_2-field [29].

Table 1
Comparison of timings between vortex method and pseudo-spectral method for the collision of two vortex tubes at $Re_\Gamma = 10,000$, on 4096 cores. We report the number of time steps to reach $T = 10$.

Method	Time per timestep (s)	Number of time steps	Time to solution (h)	Max. error in $v_{\text{effective}}$ (%)
rVM-M_4', RK3, LCFL = 0.0625	10.6	10,034	29.5	4.0
rVM-M_6^*, RK4, LCFL = 0.125	18.3	5398	27.4	2.5
PS, RK4, CFL = 0.75	14.8	7185	29.5	1.0

but the pseudo-spectral method needs to backward-transform both the vorticity and the velocity, and then forward-transforms the term $\mathbf{u} \times \boldsymbol{\omega}$.

Because of the large timesteps allowed with the vortex method the time to solution is smallest for the vortex method with M_6^*-kernel, albeit at the cost of a larger error. We note that the timings presented here are very dependent on the flow case and computational settings. In fact, if we would double the resolution of this computation, the number of time steps required for the pseudo-spectral method increases by a factor of two due to the CFL criterion; for the vortex method, assuming that the deformation in the flow does not change much, we could use the same timestep and therefore the number of time steps remains unchanged. Furthermore, we know from the scaling properties of our code [12] that the Fast Fourier Transforms (FFTs) are the main limitation in the scalability. Since the pseudo-spectral method performs more FFTs per time-step than the vortex method, we expect a better scaling behavior for the vortex method at a larger number of cores.

5. Conclusions

We have compared the remeshed vortex method with a pseudo-spectral method in simulations of a Taylor–Green vortex at $Re_\Gamma = 1600$ and two colliding vortex tubes at $Re_\Gamma = 10,000$. For both studies, the vortex method resolves the flow qualitatively well when the third order M_4'-kernel is used for interpolation between the particles and the mesh. When the kernel is replaced by the fourth order M_6^*-kernel, the results of the vortex method match the results computed by the pseudo-spectral method also quantitatively in all but the smallest length scales.

For the high Reynolds flow case, we have established the remeshed vortex method as a fast and accurate alternative to the pseudo-spectral method.

Acknowledgments

References

[1] L. Rosenhead, The formation of vortices from a surface of discontinuity, Proceedings of the Royal Society of London, Series A 134 (1931) 170–192.
[2] A.J. Chorin, Numerical study of slightly viscous flow, Journal of Fluid Mechanics 57 (4) (1973) 785–796.
[3] A. Leonard, Review: vortex methods for flow simulation, Journal of Computational Physics 37 (1980) 289–335.
[4] A. Leonard, Computing three-dimensional incompressible flows with vortex elements, Annual Review of Fluid Mechanics 17 (1985) 523–559.
[5] C. Anderson, C. Greengard, On vortex methods, SIAM Journal on Numerical Analysis 22 (3) (1985) 413–440.
[6] P. Koumoutsakos, Inviscid axisymmetrization of an elliptical vortex, Journal of Computational Physics 138 (2) (1997) 821–857.
[7] G.H. Cottet, P. Koumoutsakos, Vortex Methods: Theory and Practice, Cambridge University Press, 2000.
[8] G. Winckelmans, Vortex methods, in: E. Stein, R. De Borst, T.J. Hughes (Eds.), Encyclopedia of Computational Mechanics, vol. 3, John Wiley and Sons, 2004.
[9] P. Koumoutsakos, Multiscale flow simulations using particles, Annual Review of Fluid Mechanics 37 (2005) 457–487.
[10] L. Greengard, V. Rohklin, A fast algorithm for particle simulations, Journal of Computational Physics 73 (2) (1987) 325–348.
[11] M. Bergdorf, P. Koumoutsakos, A. Leonard, Direct numerical simulations of vortex rings at $Re_\Gamma = 7500$, Journal of Fluid Mechanics 581 (2007) 495–505.
[12] P. Chatelain, A. Curioni, M. Bergdorf, D. Rossinelli, W. Andreoni, P. Koumoutsakos, Billion vortex particle direct numerical simulations of aircraft wakes, Computer Methods in Applied Mechanics and Engineering 197 (2008) 1296–1304.
[13] G.H. Cottet, B. Michaux, S. Ossia, G. VanderLinden, A comparison of spectral and vortex method in three-dimensional incompressible flows, Journal of Computational Physics 175 (2002) 702–712.
[14] R. Cocle, L. Bricteux, G. Winckelmans, Scale dependence and asymptotic very high reynolds number spectral behavior of multiscale subgrid models, Physics of Fluids 21 (8) (2009).
[15] J. Williamson, Low-storage Runge–Kutta schemes, Journal of Computational Physics 35 (1980) 48–56.
[16] P. Koumoutsakos, Inviscid axisymmetrization of an elliptical vortex, Journal of Computational Physics 138 (2) (1997) 821–857.
[17] I. Sbalzarini, J. Walther, M. Bergdorf, S. Hieber, E. Kotsalis, P. Koumoutsakos, PPM — a highly efficient parallel particle-mesh library, Journal of Computational Physics 215 (2) (2006) 566–588.
[18] J. Monaghan, Extrapolating B splines for interpolation, Journal of Computational Physics 60 (2) (1985) 253–262.
[19] M. Bergdorf, Multiresolution Particle Methods for the Simulation of Growth and Flow, Ph.D. Thesis, ETH, Zürich, 2007.
[20] T. Hou, R. Li, Computing nearly singular solutions using pseudo-spectral methods, Journal of Computational Physics 226 (2007) 379–397.
[21] J.P. Boyd, Chebyshev and Fourier spectral methods, second ed., Dover Publications, New York, 2000.
[22] C. Canuto, M.Y. Hussaini, A. Quarteroni, T.A. Zang Jr., Spectral Methods. Fundamentals in Single Domains, Springer-Verlag, Berlin, 2006.
[23] C. Canuto, M.Y. Hussaini, A. Quarteroni, T.A. Zang Jr., Spectral Methods. Evolution to Complex Geometries and Applications to Fluid Dynamics, Springer-Verlag, Berlin, 2007.
[24] M.E. Brachet, D. Meiron, S.A. Orszag, B. Nickel, R.H. Morf, U. Frisch, Small-scale structure of the Taylor–Green vortex, Journal of Fluid Mechanics (1983).
[25] M.V. Melander, F. Hussain, Cut-and-connect of two antiparallel vortex tubes, in: Proceedings of the 1988 CTR Summer Program, 1988, pp. 257–286.
[26] D. Virk, F. Hussain, R. Kerr, Compressible vortex reconnection, Journal of Fluid Mechanics 304 (1995) 47–86.

[27] G. Carnevale, M. Briscolini, R. Kloosterziel, G. Vallis, Three-dimensionally perturbed vortex tubes in a rotating flow, Journal of Fluid Mechanics 341 (1997) 127–163.
[28] G. Winckelmans, A. Leonard, Contributions to vortex particle methods for the computation of three-dimensional incompressible unsteady flows, Journal of Computational Physics 109 (1993) 247–273.
[29] J. Jeong, F. Hussain, On the identification of a vortex, Journal of Fluid Mechanics 285 (1995) 69–94.